Study on Integration of Remote Sensing for Predicting Complicated Forest Fire Spread

Pingbo Liu * and Gui Zhang

Posted Date: 20 August 2024

doi: 10.20944/preprints202408.1458.v1

Keywords: forest fire spread; Wang Zhengfei model; remote sensing; prediction

 doi:10.20944/preprints202408.1458.v1

Article

Study on Integration of Remote Sensing for Predicting Complicated Forest Fire Spread

Pingbo Liu [1,2,*] and Gui Zhang [1]

[1] College of Forestry, Central South University of Forestry and Technology, Changsha 410004, China; zgui@csuft.edu.cn (G.Z.);
[2] College of Computer Science and Mathematics, Central South University of Forestry and Technology, Changsha 410004, China
* Correspondence: liupingbo@csuft.edu.cn

Abstract: Forest fires can occur suddenly and have significant environmental, economic, and social consequences. Timely and accurate evaluation and prediction of their progression, particularly the spread speed in difficult-to-access areas, are essential for emergency management departments to proactively implement prevention strategies and scientifically extinguish fires. This paper provides a comprehensive analysis of advanced technologies for predicting forest fire spread in China and globally. Incorporating remote sensing (RS) technology and forest fire science as the theoretical foundation, and utilizing the Wang Zhengfei forest fire spread model as the technical framework, this study constructs a forest fire spread model based on remote sensing interpretation. The model optimizes the method for acquiring parameters and enhances algorithm accuracy. By considering regional landforms (ridge lines, valley lines, slopes) and vegetation coverage, this paper establishes visual interpretation markers for identifying hotspots within the spread model. Utilizing statistical data from pixels within the fire line zone transforms the methodology for predicting forest fire spread speed, resulting in greater accuracy compared to conventional fixed-point predictions. Finally, the model was applied to the case of a forest fire in Mianning County, Sichuan Province, China and verified using high-time resolution mid-infrared image data and previous research findings. The results demonstrate that the predicted fire spread area from this RS-enabled model is consistent with both high-time resolution geostationary satellite data and previous research outcomes, indicating high reliability. This model can provide crucial fire spread information to relevant emergency departments, enabling effective preemptive measures and scientific firefighting strategies.

Keywords: forest fire spread; Wang Zhengfei model; remote sensing; prediction

1. Introduction

Forests, the largest terrestrial ecosystems on Earth, are essential for maintaining global ecological balance, stabilizing the climate, conserving biodiversity, and providing resources crucial for human life. As human society evolves, the planet is witnessing a surge in extreme climates, resulting in a heightened frequency of forest fires globally. China also faces heightened fire danger levels and challenges in firefighting. The majority of China's landmass lies in the mid-latitude zone, where there are clear seasonal variations. Spring weather conditions are characterized by low humidity levels, increasing the risk of wildfires, and the specific landscape and wind conditions pose difficulties in fire suppression efforts once ignited. Forest fires typically occur unexpectedly and spread fast and can lead to significant impacts to environment, economy, and society. Timely and accurate evaluation and prediction of the progression patterns, particularly the forest fire spreading speed in those difficult-to-access areas, are essential for emergency management departments to proactively implement prevention strategies and put out fires scientifically.

 doi:10.20944/preprints202408.1458.v1

Various models are commonly used to predict the spread of forest fires. For accurate predictions, it is essential to have precise parameters or information for the models. However, these required parameters are often unknown or difficult to ascertain, and much of the data used are based on experience or historical records.

The fundamental concept behind establishing a forest fire spread model involves mathematically processing various factors related to forest fire spread under simplified conditions. This approach derives relationships between these factors and the predicted outcomes. Using these relationships, the model characterizes the speed and other features of the temporal and spatial evolution of forest fires, thereby predicting their subsequent spread. Presently, various forest fire spread models (detailed in the data and methods section) have been studied globally.

In recent years, the rapid advancement of satellite remote sensing (RS) technology has overcome the high costs, complexity, and limitations of all-weather, all-directional, real-time monitoring associated with traditional forest fire monitoring methods, and making RS an increasingly vital tool for surveillance. Emerging in the 1960s, RS technology is less constrained by ground conditions, offers a wide detection range, quickly obtains information, and is cost-effective. It allows for accurate positioning of ground objects and currently plays an important role in fields such as environmental monitoring, urban planning and development, emergency response, and disaster management. However, current research on forest fire RS primarily focuses on monitoring and post-disaster assessment. Fire emergency departments rely primarily on individual systems and video surveillance data to comprehend the fire scenario and base their firefighting strategies mostly on practical knowledge, rather than precise fire spread positioning and scientific fire trend analysis [1]. The RS technology has rarely been used in the prediction of the fire spreading.

Because of unique capability of RS in the fast, and sometimes real-time, transmission of information, integrating RS data into fire prediction models is expected to significantly enhance prediction accuracy. This integration can provide critical fire spread data for relevant fire emergency departments to effectively deploy needed defense proactively and manage fire scientifically.

The objective of the present paper is to evaluate the effectiveness of using the RS data to improve fire spreading prediction. By combining the high-resolution satellite RS data, advanced interpretation technology, and an improved Zhengfei Wang forest fire spread model, the speed and area of forest fires spreading is determined. The enhanced accuracy and reliability of the RS-enabled forest fire spreading model are demonstrated.

2. Data and Methods

In this paper, we first selected a model that is widely used for predicting the fire spreading in China, and identified the necessary information or environmental parameters required for accurate prediction of forest fire spreading. We then retrieved and analyzed the RS data from publicly available reliable sources, extracted the needed information for the selected model for forest fire spreading prediction. By integrating the extracted and analyzed RS data to the forest fire spreading model, the improved prediction of RS enabled forest fire spreading is achieved.

To best evaluate the accuracy of the RS-enabled fire spreading prediction, we selected a large, severe forest fire that occurred in Sichuan Province, China, in 2021 and calculated the fire spread speed in various locations and conditions using RS-enabled fire spreading prediction model, and compared the calculated results with data from reliable resources (the fire point monitoring results and historical archives).

2.1. Model Selection and improvement for Forest Fire Spreading

To evaluate the benefits of integrating the RS into forest fire spreading models, a reliable model for predicting the specific areas susceptible to forest fires is essential. Currently, several classic forest fire spread models are widely used, including the Canadian Forest Fire Danger Rating System [2], the McArthur model from Australia [3], the Rothermel model from the USA [4], and the Wang Zhengfei model from China [5]. The model from the Canadian forest fire risk prediction system focuses on the impact of slope on spread speed, but its accuracy decreases in scenarios that deviate

 doi:10.20944/preprints202408.1458.v1

from experimental conditions. In Australia, the McArthur model proposed by Noble I.R. determines the fire spread speed solely by meteorological factors such as wind speed and fire danger indexes, neglecting the impact of the combustibles themselves. The spread model proposed by Rothermel in the USA is based on the physical mechanism of the conservation of energy law, integrating wind speed, slope, and combustible information. While practical, this model requires many parameters that are difficult to obtain and has stringent requirements on combustibles—needing a uniform state of combustibles, making it suitable only for predicting spread speed in a single direction.

The Wang Zhengfei model, developed in China, incorporates wind speed, slope, and types of combustibles [5], and is noted for its broad adaptability in China. The fire spread prediction of the Wang Zhengfei model is shown in Formula (1).

$$\mathrm{R} = R_0 K_S K_W / \cos\varphi, \tag{1}$$

where R is the estimated fire spread speed (m/min), $\mathrm{R_0}$ is the initial spread speed (m/min), $\mathrm{K_S}$ is the correction factor of type of combustibles, which is a constant that varies with time and locations, $\mathrm{K_W}$ is wind correction factor, and $\mathrm{K_\varphi}$ is slope correction factor.

Mao et al. considered the combination of terrain and wind direction to improve the slope influence factor $\mathrm{K_\varphi}$, and derived equations for five directions: up slope, left level slope, right level slope, down slope, and wind direction, thus enhancing the model's practical applicability [6]. Zhang and Liu incorporated the impact of combustible moisture on the speed of fire spread [7], which improved the calculation of the slope correction factor and initial spread speed, resulting in a more accurate prediction of fire spread speed. By considering the effects of the terrain and wind direction as well as the combustibles moistures, the improved prediction models for fire spread are detailed in Equations (2)–(6).

Uphill: $\mathrm{R} = R_0 \times K_S \times K_\omega \times K_\varphi = 1.0372 \times e^{-0.057m} \times K_S \times e^{0.1783v\cos\theta} \times 0.6172e^{0.0805w}$ (2)

Downhill: $\mathrm{R} = R_0 \times K_S \times K_\omega \times K_\varphi = 1.0372 \times e^{-0.057m} \times K_S \times e^{0.1783v\cos(180-\theta)} \times (0.0249\omega + 1)$ (3)

Leftward: $\mathrm{R} = R_0 \times K_S \times K_\omega \times K_\varphi = 1.0372 \times e^{-0.057m} \times K_S \times e^{0.1783v\cos(\theta+90^\circ)}$ (4)

Rightward: $\mathrm{R} = R_0 \times K_S \times K_\omega \times K_\varphi = 1.0372 \times e^{-0.057m} \times K_S \times e^{0.1783v\cos(\theta-90^\circ)}$ (5)

Wind direction: $\mathrm{R} = R_0 \times K_S \times K_\omega \times K_\varphi = 1.0372 \times e^{-0.057m} \times K_S \times e^{0.1783v} \times 0.6172e^{0.0805w}$ (6)

where m is the moisture of the combustibles, v is the wind speed, θ is the angle between the wind direction and the uphill direction, and ω is the slope.

In the models developed by Wang Zhengfei and then improved by others, the temperature effect was not considered, which introduces some limitations in fire spread prediction. As altitude increases, the temperature within the forest gradually decreases, the relative humidity incrementally increases, and the moisture content of the ground cover also becomes higher, making the combustibles less flammable. Additionally, in subalpine zones or near watersheds, precipitation noticeably increases, further reducing the likelihood of forest fires. In mountainous conditions, with every 100m increase in altitude, the temperature decreases by 0.6℃ [8]. The higher the altitude, the lower the temperature, the greater the relative humidity, the higher the moisture content of the ground cover, and the more significant the increase in precipitation, generally reducing the likelihood of fires.

This paper builds on the above existing models and incorporates the effects of the temperature on the fire spread. In calculating the fire spread speed using the models, the combustibles moisture content was based on specific conditions of the selected area and actual satellite RS data obtained at various times during the fire's occurrence and development. Other necessary information for predicting the fire spread was also retrieved from the RS data (to be detailed later). It is expected that by incorporating actual RS data and temperature effects, the prediction of the fire spread will be more accurate and reliable.

 doi:10.20944/preprints202408.1458.v1

2.2. Remote Sensing

2.2.1. Moisture of Combustibles

The methods for estimating vegetation moisture content using optical RS technology generally rely on parameters and models such as spectral reflectance, vegetation water index, and radiative transfer models. In this paper, the moisture content of combustibles in forest areas is estimated based on spectral analysis and the angle slope index.

Williams found that hydroxyl groups in water produce diagnostic absorption spectra in the spectra of liquid water, moist soil, and moist vegetation, with the fundamental absorption spectrum occurring around 3000nm and several strong absorptions in the shortwave infrared range of 1300~2500nm [9]. Carter's research on leaf absorption bands in the shortwave infrared spectrum discovered that leaf reflectance sensitivity to water content is highest at the spectral bands of 1450, 1950, and 2500nm within the 1300~2500nm range [10]. Based on the correlation between spectral reflectance and vegetation water content, Deng et al. found good correlations between vegetation water content and spectral reflectance in the visible red light band (620~700nm) and near-infrared bands (800~1350, 1600~1950, 2200~2400nm) [11]. The angle slope index, proposed by Palacios-Orueta and Khanna, uses the geometric shape of the spectra across three consecutive bands to describe the relationships among these spectra, thus detecting not only the reflectance values of any band but also the relationships between bands [12]. The range of wavelengths affected by water's refraction and absorption spans approximately several hundred nanometers [10,13], with strong correlations between individual bands in spectral imagery. The relationship of wavelengths between bands is as significant as reflectance in spectral data, under which premise the angle slope index is expected to more accurately represent the relationship between spectral reflection and water content. The angle slope index includes the shortwave angle normalized index (SANI), the shortwave angle slope index (SASI), and the near-infrared angle index (ANIR), initially focused on the three consecutive MODIS bands NIR, SWIR1, and SWIR2, characterizing their interrelationships, and later introduced the near-infrared angle index ANIR (Figure 1 and Equation (7)), characterizing the relationships between the RED, NIR, and SWIR1 bands [12].

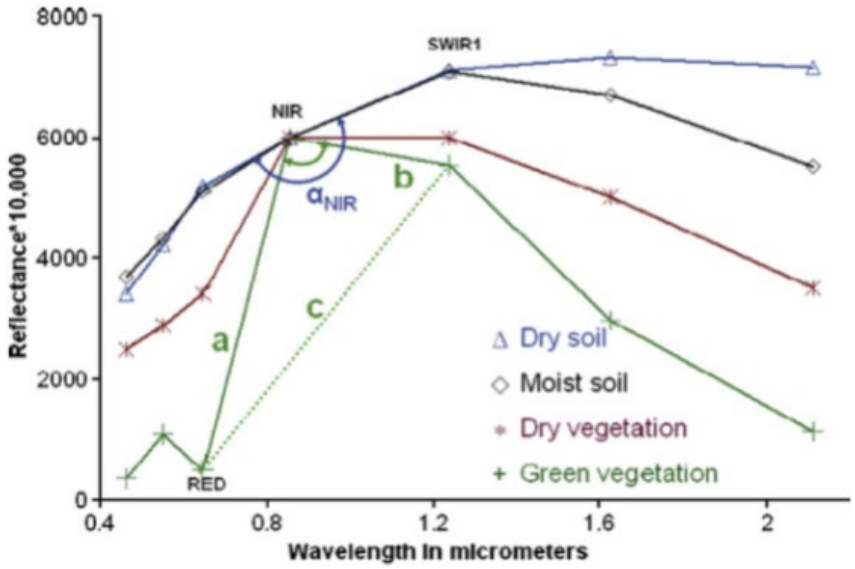

Figure 1. The angle, α_{NIR} formed at the NIR by the reflectances at bands, Red, NIR and SWIR1. An additive offset was applied to make spectral values equal at NIR band (adapted from Shruti Khanna et al. [12]).

Based on the angle slope index, a new leaf equivalent water thickness (LEWT) inversion model was developed by Lei et al. using the improved distance projection ratio index (DPRI2), which in turn was used to invert the canopy equivalent water thickness (CEWT) [14]. Deng et al., through improvements to the original angle slope index, proposed two new angle slope indices: the near-

 doi:10.20944/preprints202408.1458.v1

infrared angle normalized index (NANI, see Equation (8)) and the near-infrared angle slope index (NASI, see Equation (9)), which enhanced the accuracy in the inversion of vegetation water content. It was shown that the linear regression model established with the ANIR index exhibits the highest fit, with a coefficient of determination 0.791 and an RMSE of 0.047 [11].

$$\mathrm{ANIR}_{(\alpha_{\mathrm{NIR}})} = cos^{-1}\left[\frac{a^2+b^2-c^2}{2ab}\right], \tag{7}$$

$$\mathrm{NANI} = \mathrm{ANIR} \times \frac{SWIR1-RED}{SWIR1+RED}, \tag{8}$$

$$\mathrm{NASI} = \mathrm{ANIR} \times (\mathrm{SWIR1} - \mathrm{RED}), \tag{9}$$

where a, b, and c denote the distances as shown in Figure 1, αNIR the angle between the RED-NIR and NIR-SWIR1 of the reflectance spectral curve.

Herein, the moisture content of combustibles in the fireline area was estimated based on the infrared angle indices ANIR and NANI.

2.2.2. Slope of the Fire Area

Slope is the degree of inclination of the local surface in space, and its magnitude directly affects the spread speed of forest fires, making it an important factor in studying forest fire spread. The Digital Elevation Model (DEM), as one of the core databases of the Geographic Information System (GIS) spatial database [9–11], is fundamental for conducting two-dimensional spatial simulations of terrain and generating topographic maps. Therefore, a reasonable slope and aspect algorithm is essential for terrain analysis models. Strictly speaking, the slope at any point on the surface is defined as the angle between the tangent plane passing through that point and the horizontal surface, showing the degree of inclination of the surface at that point. Numerically, it is equal to the angle between the normal vector $\vec{n}$ of the surface differential element passing through that point and Z. When extracting slope specifically, a simplified differential formula is commonly used, with the complete mathematical expression being:

$$\mathrm{Slope} = \arctan\sqrt{f_x^2 + f_y^2}, \tag{10}$$

where f_x is the rate of elevation change in the north-south direction, and f_y is the rate of elevation change in the east-west direction. Equation (10) can be used to calculate the slope at a point on the ground, with the key being the calculation of f_x and f_y. Grid DEM represents the terrain surface in a discrete form and the surface function is generally unknown, so f_x and f_y are typically calculated locally through numerical differentiation methods or local surface fitting methods.

Currently, the mainstream methods for extracting terrain information based on DEM include six types: second-order differential method, Frame differential algorithm, third-order unweighted differential algorithm, third-order inverse-distance-squared weighted differential algorithm, third-order inverse-distance weighted differential algorithm, and simple differential algorithm [15–17] (see Table 1).

Table 1. Mathematical Models of Slope and Aspect Calculation *.

Method of calculation	f_x	f_y
Simple Difference	$(z_5 - z_2)/g$	$(z_5 - z_4)/g$
second order difference	$(z_8 - z_2)/(2g)$	$(z_6 - z_4)/(2g)$
Frame difference	$(z_7 - z_1 + z_9 - z_3)/(4g)$	$(z_3 - z_1 + z_9 - z_7)/(4g)$
third order unweighted difference	$(z_7 - z_1 + z_8 - z_2 + z_9 - z_3)/(6g)$	$(z_3 - z_1 + z_6 - z_4 + z_9 - z_7)/(6g)$
third order inverse distance weighted difference	$(z_7 - z_1 + 2(z_8 - z_2) + z_9 - z_3)/[(4 + 2\sqrt{2})g]$	$(z_3 - z_1 + 2(z_6 - z_4) + z_9 - z_7)/[(4 + 2\sqrt{2})g]$

 doi:10.20944/preprints202408.1458.v1

third order inverse square distance weighted difference.	$(z_7 - z_1 + 2(z_8 - z_2) + z_9 - z_3)/(8g)$	$(z_3 - z_1 + 2(z_6 - z_4) + z_9 - z_7)/(8g)$

*: g represents the grid resolution, z_i(i=1, 2, 3, ..., 9) represents the elevations of the grid points around the center point, and both f_x and f_y are calculated for each center point [18,19].

Hao et al. [20], based on DEMs of three different terrains, calculated slope and aspect using six methods and analyzed that the third-order differential series algorithms are quite applicable. The Frame differential performed well in the Dongjiang Basin and the source region of the Yellow River [18]. Chen et al. [21], using the loess hilly gully region as a case study, studied the applicability of six slope extraction algorithms, using the standard deviation, maximum value, and slope grading area data extracted by the six different algorithms as statistical indicators, and employed one-way analysis of variance to explore the scope of application of the six algorithms. It was found that the third-order inverse-distance total difference and third-order inverse-distance squared total difference algorithms worked well in the loess hilly gully region. Li et al. [22] used a DEM generated from a 1:10,000 topographic map as the study object, applied six algorithms to extract slope and aspect, and analyzed the algorithms suitable for the study area by comparing maximum values, mean errors, and cumulative absolute deviations, which provided a reference for practical work based on the conclusions drawn. Jiang et al. [23], using Qingdao City in Shandong Province as a case study, calculated the slope of the study area using six different algorithms and statistically analyzed and calculated the slope matrices extracted by the different methods. The third-order differential series algorithms was found to have the highest accuracy and the lowest probability of extreme cases, being quite stable; among them, the third-order inverse-distance squared total differential and third-order inverse-distance weighted differential algorithms exhibit the highest accuracy under various statistical indicators. Meanwhile, the simple differential, second-order differential, and Frame algorithms show various degrees of bias and extreme cases under different statistical indicators.

With the above context, the third-order inverse-distance squared total differential method was selected in this paper, and a 3×3 local moving window size was used for calculation. Table 1 shows that mathematical model for calculating slope and aspect.

2.2.3. Fire Spot Pixel

The Gaofen-4 satellite is capable of performing minute-level, high-frequency, continuous repetitive observations of the same area, and can also rapidly adjust its pointing to the observation area within minutes. Previous research has shown that the optimal detection center wavelength for the spectral characteristics of burning wooden materials is between 3620~4830nm. Regardless of the presence of visible flames, the mid-infrared imagery of the Gaofen-4 satellite effectively detects high-temperature forest fire spots. The 400m resolution mid-infrared imagery can penetrate smoke to identify visible flames. Herein the mid-infrared channel of Gaofen-4 was used to invert fire spot pixels and to validate the simulation results of the forest fire spread model. An adaptive threshold monitoring algorithm for fire spots, constructed using the "split window method," captures anomalous brightness temperatures in RS imagery. The specific algorithm is as follows:

1. Calibrate the image DN value to the thermal radiance $L_e(\lambda_i)$

$$L_e(\lambda_i) = Gain \cdot DN + offset, \tag{11}$$

where $Le(\lambda i)$ is the radiance, DN is the image grayscale value, Gain is the gain coefficient, it represents the proportional relationship between the DN and the thermal radiance value, and offset is the absolute calibration coefficient offset value, which is for adjusting the converted radiation brightness value to ensure that it is closer to the true radiation.

2. Use the Planck function to solve for the brightness temperature on the star

$$T = \frac{K_{i2}}{\ln(1+K_{i1}/L_e(\lambda_i))}, \tag{12}$$

 doi:10.20944/preprints202408.1458.v1

where K_{i1} and K_{i2} are constants, $K_{i1} = 2h' \cdot c^2/(\lambda_i{}^5)$, $K_{i2} = h' \cdot c/(k \cdot \lambda_i)$; h′ is Planck constant $6.626 \cdot 10^{-34} J \cdot s$; c is the speed of light, $2.998 \cdot 10^8 m/s$; k is the Boltzmann constant, approximately $1.38 \cdot 10^{-23} J \cdot K^{-1}$.

3. Discrimination of fire point pixels

Combine with the land cover type map, pixels in the forested area with a brightness temperature greater than 315 K are designated as high-temperature suspect pixels. Set these high-temperature suspect pixels as the center of the initial window, with the initial window size set to 7×7. Calculate the variance and average of the brightness temperature of the background pixels within the window; during calculation, use the forest NDVI mask operation to exclude other high-temperature suspect pixels from the background pixels. If the number of background pixels within the window is less than 20% of the total number of pixels in the window, then expand the window successively to 9×9, 11×11, ..., 21×21; if it still does not meet the requirements, abandon the judgment of that pixel and mark it as a non-fire pixel. If the suspect pixel meets the conditions of Equation (13), then the pixel is determined to be a fire pixel [24].

$$T > T_{bg} + 3\delta T_{bg}, \tag{13}$$

where T_{bg} is the average brightness temperature of background pixel, δT_{bg} is the standard deviation T_{bg}.

Himawari-8 satellite was equipped with the advanced imager AHI, the temporal resolution of the entire observation is 10 min once, the spatial resolution of the mid infrared is 2km (channel 7) [25]. According to Planck's law, the difference in radiation brightness results in that even if the fire area only accounts for 1/104-1/103 of the total area of the pixel, the brightness temperature value of the fire point pixel in the mid-infrared band will be significantly increased, and there is a significant difference with the surrounding pixel. In the far infrared band, this difference in brightness temperature also occurs, but the difference is smaller. This characteristic of bright temperature difference can be used as the main basis for fire point identification. The method of discriminating the fire point pixel of the algorithm in this study is as followings [26]:

Daytime: Those who meet the conditions{A or [B and C and D and (E or F)]} are recognized to be a fire, otherwise it is a non-fire.

Night: Those who meet the conditions [A or (B and C and D)] are recognized to be a fire point, otherwise it is a non-fire spot.

A: $T7 > 360K (Night 320K)$

B: $\Delta T > \Delta\overline{T} + 3.5\delta_{\Delta T}$

C: $\Delta T > \Delta\overline{T} + 6K$

D: $T_7 - \overline{T}_7 > 2\delta_7$

E: $T_{14} - \overline{T}_{14} > 2.5\delta_{14}$

F: $\delta_7^{'} > 5K$

In the formula, $T7$ and $T14$ are Himawari-8 data 3.9μm and 11.2μm channel temperature. $\overline{T}_7$ and $\overline{T}_{14}$ are the average temperature of 3.9μm and 11.2μm in the background window. ΔT is the temperature difference between 3.9μm and 11.2μm. $\Delta\overline{T}$ is the average temperature difference between 3.9μm and 11.2μm in the background window. δ_7 and δ_{14} are the temperature standard deviations of 3.9μm and 11.2μm in the background window. $\delta_{\Delta T}$ is the standard deviation of the temperature difference between 3.9μm and 11.2μm in the background window. $\delta_7^{'}$ is the 3.9μm standard deviation of the fire point pixel in the background window.

2.3. Integration of RS and Fire Spreading Model

At the onset of a forest fire, satellite RS data capable of monitoring the fire was obtained and preprocessed for inversion of model parameters. In this study, Sentinel-2 satellite data were used to

 doi:10.20944/preprints202408.1458.v1

invert the moisture content of combustibles in the fire-affected area, 30-meter STER GDEM data to invert terrain slope, and Gaofen-4 and Himawari-8 data to capture abnormal brightness temperatures. Based on the vegetation cover data of the fire area, instantaneous meteorological data (wind speed, wind direction) and the moisture and slope information of each pixel along the fire line, the speed of the fire that can spread in the potential direction was calculated. The maximum value in the possible spread direction was determined based on the statistical data of the spread speed. Under the premise of relatively stable meteorological data, minor changes in slope, and consistent forest types, the area that the fire line can reach after a certain period based on the maximum speed was estimated, which would provide a basis for firefighting. Finally, the fire spot pixels captured by Gaofen-4, Himawari-8 data and historical archive data were used to validate the results of the RS enabled fire spread predictions. The specific flow of the model simulation is shown in Figure 2.

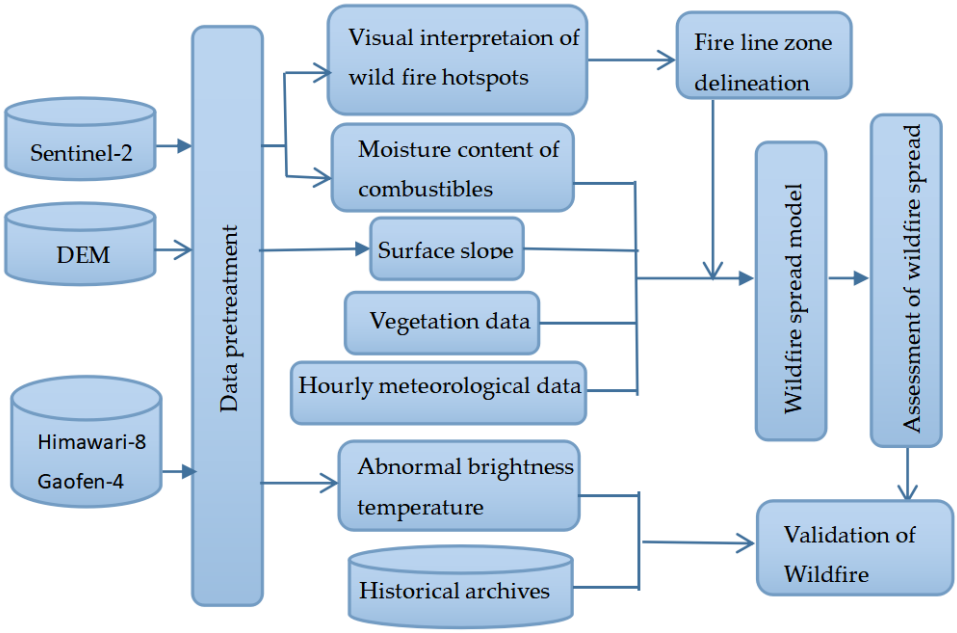

Figure 2. Technical route of forest fire spread simulation based on RS interpretation.

2.4. Data sources for Remote Sensing Interpretation

Multispectral data from Sentinel-2 were selected to estimate the moisture content of combustibles, while Himawari-8 and Gaofen-4 captured temperature anomalies. Data from Sentinel-2, S2B_MSIL1C_20210424T034529_N0300_R104_T48RTS_20210424T053845, were downloaded from the European Space Agency (ESA) Copernicus Data Centre (https://scihub.copernicus.eu/dhus/#/home), accessed on April 24, 2021. Using the Sen2Cor 2.5.5 software [8], the L1C level products are radiometrically calibrated and converted into L2A level products. After preprocessing (mainly including geometric correction and atmospheric correction), the S2 images are projected in UTM Zone 48 WGS84 and resampled to a spatial resolution of 10m. Data from Gaofen-4, GF4_IRS_E103.0_N29.3_20210423_L1A0000374570 were downloaded from China Center for Resources Satellite Data and Application (http://www.cresda.com/CN/), accessed on April 24, 2021. The full-scale observation data of Himawari-8 L1 NC (Network Common Data Format) were downloaded from the Japan Meteorological Agency(https://www.eorc.jaxa.jp/ptree/index.html). Using Sentinel-2 satellite imagery and DEM data for orthorectification and precise geometric correction. The 30-meter STER GDEM data come from the Geospatial Data Cloud (https://www.gscloud.cn). The 30-meter resolution land cover type data n48_25_2020lc030 were obtained from National Geomatics Center of China.

The hourly meteorological data of Mianning county on April 24, 2021 were obtained from ERA5 hourly data on single levels from 1979 to present dataset. ERA5 (ECMWF Re-Analysis 5) represents the fifth generation of reanalysis data by the European Centre for Medium-Range Weather Forecasts

 doi:10.20944/preprints202408.1458.v1

(ECMWF), which provides numerical data on global climate and weather over the past 40 to 70 years, as shown in Table 2. The softwares used mainly include ENVI5.3、Arc GIS10.2 and MATLAB.

Table 2. Hourly meteorology of Mianning County on April 24, 2021.

Time (UTC)	Wind direction	Wind speed (m/s)
3:00	northward	1.23
	westward	0.81
4:00	northward	1.44
	westward	0.78
5:00	northward	1.48
	westward	0.54
6:00	northward	1.39
	westward	0.34
7:00	northward	1.22
	westward	0.10

2.5. A Specific Fire for Comparing and Evaluating the RS Enabled Fire Spreading

To compare the accuracy of the RS enabled forest fire prediction, a forest fire that occurred in Mianning County (it is called Mianning Fire afterwords in this paper) of Sichuan province of China in April, 2021 was used. Mianning was located in the northeastern part of the Liangshan Yi Autonomous Prefecture, between 28°5′N and 29°2′N latitude, and 101°38′E to 102°19′E longitude, as shown in the Figure 3. The Mianning county has a forest cover rate of 34.7% which is rich in different species, including a total of 140 families, 341 genera, and 608 species of trees, shrubs, and herbaceous plants. It is situated in the middle of the Hengduan Mountains and features complex terrain and significant elevation differences, with a high mountain canyon area that fosters a unique dry-hot valley climate. The time from March to May every year is the dry-hot season. In the three months before the arrival of the main southwest monsoon in June, it is both dry and hot, making it highly susceptible to forest fires. Once a forest fire occurs in such a place, it is often at a high altitude with steep terrain, and the wind direction on the mountain can change abruptly, making firefighting dangerous and arduous due to the interplay of monsoons, mountain winds, and valley winds with high-altitude airflows. Therefore, real-time and accurate remote sensing monitoring of forest fires is urgently and vitally important for guiding emergency fire responses and scientific firefighting efforts.

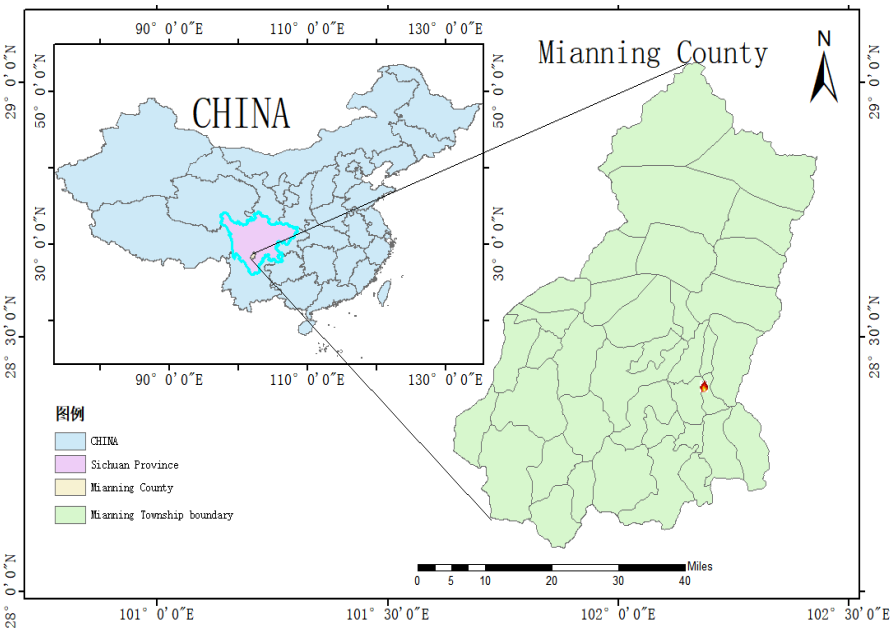

 doi:10.20944/preprints202408.1458.v1

Figure 3. Forest fire area in Mianning County, Sichuan in April 2021.

Based on the reliable resources from historical reports of the People's Government of Liangshan Yi Autonomous Prefecture and publicly available research papers, Mianning forest fire started on April 20, 2021. The majority of the fire area consisted of primary forest, with vegetation coverage exceeding 80%, primarily composed of eucalyptus and other broadleaf forests. The area features crisscrossing ravines and steep mountain slopes. Some sections are filled with cliffs and are difficult to access, characterizing a typical high mountain canyon terrain. Figure 4 shows the area where the fire occurred. The Mianning fire has been classified as a major forest fire case in China.

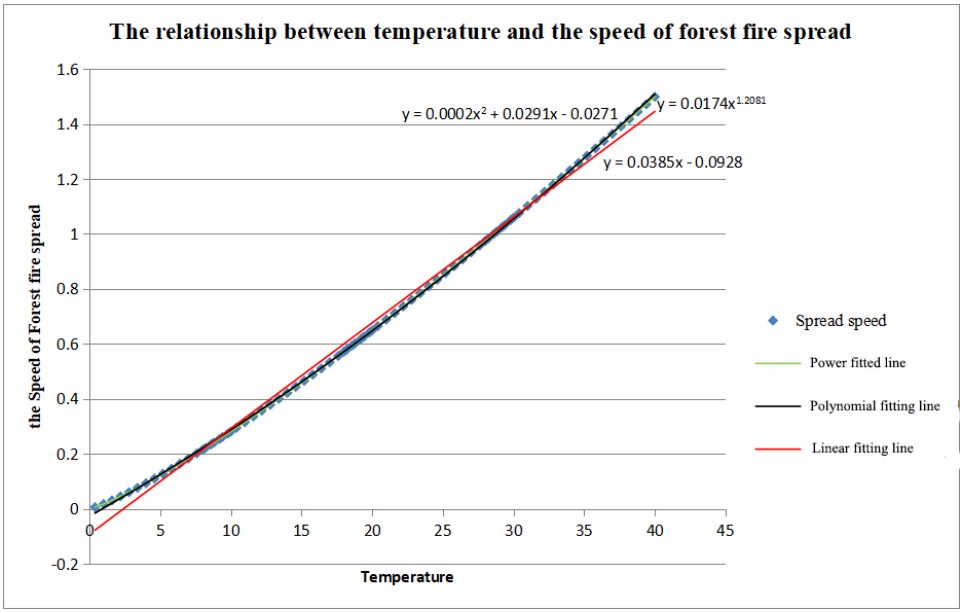

Figure 4. Relationship of temperature and fire spread speed.

Because of its challenges for putting out this fire, we consider that this Mianning fire is a good example to evaluate the accuracy for the RS enabled forest fire prediction.

According to historical records in the literature, on the night of the April 23rd, 2021, the fire site was suddenly impacted by strong winds of force 8 on the Beaufort scale (as reported by on-site meteorological data). A sudden spot fire broke out on the southern side of the western line of the original fire, which was beyond the range that could be controlled. This triggered a new fire on the northern side of Tuobie Mountain Ridge and near the western side of Baifen Mountain, creating a new fire site. The fire expanded rapidly, spreading south and north, merging with the original fire site. By April 24th, 2021, the burned area had expanded significantly to the north and northwest, crossing Baifen Mountain and spreading towards Jiaguan Village. Two light blue smoke columns, with particularly noticeable growth, were clearly visible near the eastern side of Baifen Mountain. The overall shape of the fire was "L"-shaped, measuring 5.8 km in length from north to south, 3.5 km in width from east to west, covering an area of approximately 9.55 km².

On April 24th 2021 the fire intensified significantly, with unusual growth, making it a good fire case for evaluating the forest fire spread model simulation, particularly for complicated fire prediction. In this paper, T03:45 (Universal time) on April 24th 2021 was selected as the starting time node of the spread simulation.

3. Results and Discussion

3.1. Model Improvement: Temperature Effect on Fire Spreading

It has been known that the higher the altitude, the lower the temperature, and the higher the humidity or moisture content of the ground vegetation cover, suggesting that the altitude of the forest can affect the fire spreading velocity.

 doi:10.20944/preprints202408.1458.v1

The moisture content could affect the initial fire spread speed. Zhang et al. studied the relationship of water content and initial fire spread velocity, which can be given as:

$$R_0 = 1.0372 \times e^{-0.057 \times m}, \quad (14)$$

where m(%) is the moisture content of the combustibles, R_0(m/min) is the initial spread speed.

Li et al. studied the relationship of the moisture content of ground cover and average temperature, which is:

$$\mathrm{H} = 71.72 - 48.80 \log \mathrm{T}, \quad (15)$$

where H(%) is water content, and T(°C) is the average temperature.

Therefore, by using the equation of temperature effect on moisture and how the moisture affects the initial fire spread speed, we calculated the relationship between the temperature (which is affected by altitude) and the forest fire spreading, which is

$$R_0 = 61.84 / 16.15^{\log t}, \quad (16)$$

This section may be divided by subheadings. It should provide a concise and precise description of the experimental results, their interpretation, as well as the experimental conclusions that can be drawn.

Assuming the initial temperatures of 10, 20, 30, and 40, the temperature at different altitudes for each different initial temperature was shown in Table 3.

Table 3. Relationship of elevation and forest fire spread rate.

Elevation (m)	Temperature (℃)	Initial temperature (°C)			
		10	20	30	40
0	T	0.281	0.649	1.059	1.499
100	T-0.6	0.261	0.625	1.033	1.472
200	T-1.2	0.241	0.602	1.008	1.445
300	T-1.8	0.221	0.579	0.983	1.418
400	T-2.4	0.202	0.556	0.958	1.391
500	T-3.0	0.183	0.533	0.932	1.364
600	T-3.6	0.164	0.511	0.907	1.338
700	T-4.2	0.145	0.488	0.883	1.311
800	T-4.8	0.127	0.466	0.858	1.285
900	T-5.4	0.110	0.444	0.833	1.258
1000	T-6.0	0.093	0.422	0.809	1.232

The relationship of the fire spread speed and temperature can be expressed as a linear equation:

$$y=0.0385x-0.0928, \quad (17)$$

where y is the fire spread speed and x is the temperature. Because the temperature decreases 0.6°C for each 100m of elevation increase as shown in Table 3, the fire spread speed decreases 0.0231 m/min.

Assuming an initial temperature of 25°C and a spread speed of 0.870 m/min, the speed decreases by 2.7% for every 100 meters of elevation. The rate of decrease in fire spread speed at different initial temperatures is calculated as shown in Table 4.

Table 4. Fire spread speed reduction at different initial temperatures.

Initial temperature	Initial speed of fire spreading	Reduction of fire spreading (%)
10	0.292	7.91
15	0.485	4.77
20	0.677	3.41

 doi:10.20944/preprints202408.1458.v1

25	0.870	2.66
30	1.062	2.17
35	1.255	1.84
	Average	3.79±2.27

It can be seen from Table 4 that the higher the initial temperature, the slower the reduction of fire spreading. And the improved fire spreading model is shown as follows:

$$Uphill: R = R_0 * K_S * K_\omega * K_\varphi * D_{al} = 1.0372 * e^{-0.057m} * K_S * e^{0.1783v\cos\theta} * 0.6172e^{0.0805w} * (1 - d_{al} * h/100) \quad (18)$$

$$Downhill: R = R_0 * K_S * K_\omega * K_\varphi * D_{al} = 1.0372 * e^{-0.057m} * K_S * e^{0.1783v\cos(180^\circ - \theta)} * (0.0249w + 1) * (1 - d_{al} * h/100) \quad (19)$$

$$Left - flat - slop: R = R_0 * K_S * K_\omega * K_\varphi * D_{al} = 1.0372 * e^{-0.057m} * K_S * e^{0.1783v\cos(\theta + 90^\circ)} * (1 - d_{al} * h/100) \quad (20)$$

$$Rigth - flat - slope: R = R_0 * K_S * K_\omega * K_\varphi * D_{al} = 1.0372 * e^{-0.057m} * K_S * e^{0.1783v\cos(\theta - 90^\circ)} * (1 - d_{al} * h/100) \quad (21)$$

$$Wind - direction: R = R_0 * K_S * K_\omega * K_\varphi * D_{al} = 1.0372 * e^{-0.057m} * K_S * e^{0.1783v} * 0.6172e^{0.0805w} * (1 - d_{al} * h/100) \quad (22)$$

where R is the estimated fire spread speed, R_0 is the initial spread rate, K_s is the combustible material type correction factor, K_ω is the wind correction factor, K_φ is the slope correction factor, D_{al} is the elevation correction factor, m is moisture content of combustibles, v is the wind speed, θ is the angle between wind direction and uphill direction, w is slope, d_{al} is rate of decrease in fire spread speed with elevation, h is the elevation.

3.2. Remote Sensing

3.2.1. Visual Interpretation of Forest Fire Hotspots

Forest fire hotspots are typical abnormal characteristics produced by the burning of forest vegetation, including fire spots and smoke spots. Fire spots refer to the visible flames in the vegetation burning process, while smoke spots are locations where a large amount of smoke is formed due to the evaporation of the vegetation's own moisture during combustion [22]. Using 10m optical satellite imagery during a fire, true color (bands 4, 3, 2) and false color (bands 12, 11, 8A) combinations, along with information on vegetation cover and regional topography (slopes, valley lines, ridge lines), the visual interpretation markers for hotspots and key fire areas were achieved.

From the true color composite image of Mianning 4.24 forest fire (Figure 5), it can be seen that the fire area is covered by a large area of smoke. The smoke starts at the smoke point and spreads out in a band-like extension along the wind direction, gradually changing in color from dark gray to light gray. The shape is continuously distributed in a "broom-like" fashion, and it can be distinguished from cloud-covered areas based on shape, color, and the shadows of the clouds, clearly differentiated from the surrounding dark green background.

From the false color composite image of Mianning 4.24 forest fire (Figure 6), it can be seen that the fire line emerges under the smoke cover along the ridge lines and windward slopes, appearing as strip-shaped. Fire spots intermittently appear along the fire line, showing as bright red in the composite image. Burned areas appear dark brown and are "L"-shaped, distinctly differentiated from the surrounding blue vegetation and light yellow non-forested areas.

 doi:10.20944/preprints202408.1458.v1

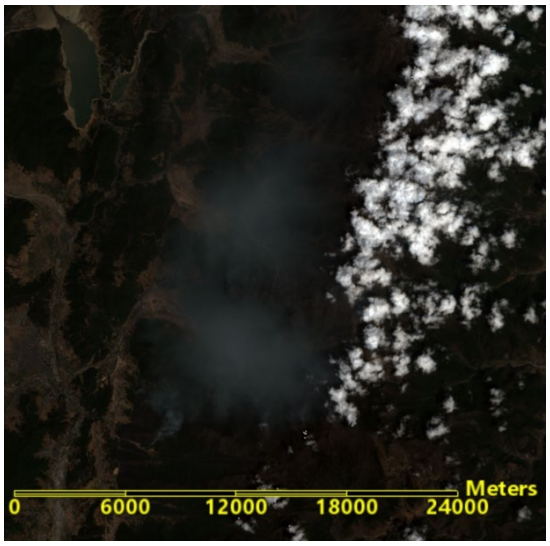

Figure 5. True color composite image of Mianning 4.24 forest fire.

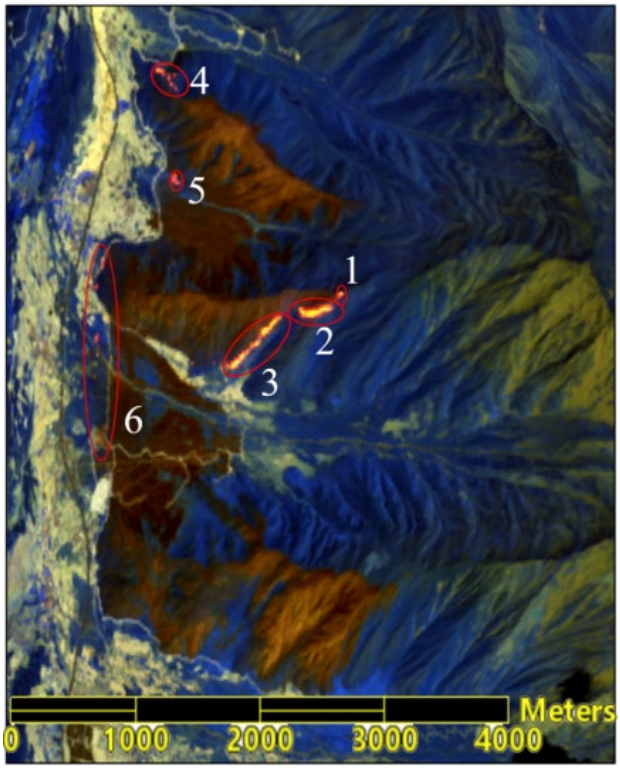

Figure 6. False color composite image of Mianning 4.24 forest fire.

By integrating Digital Elevation Model (DEM) data, the remote sensing image of the forest fire area was visualized in 3D, combined with the regional topography (slopes, valley lines, ridge lines). Six areas were identified, as shown in Figure 7. Among these, areas 1, 2, and 3 are located on the eastern side of the fire site, on the ridge, and on the sun-facing slopes, where the fire is more intense; areas 4, 5, and 6 are located on the western side of the fire site, at the base of the mountain (valley line), on the shaded slopes, where the fire is less intense.

 doi:10.20944/preprints202408.1458.v1

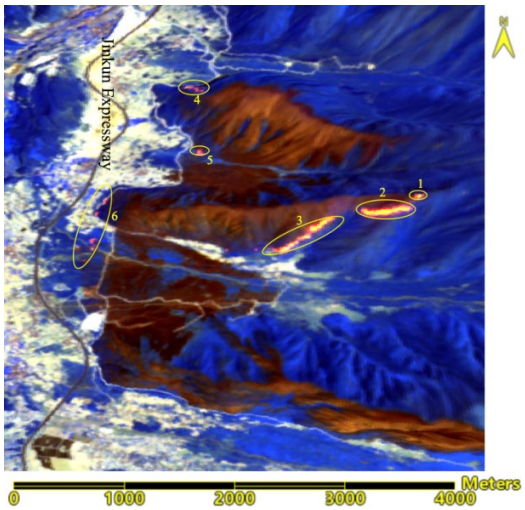

Figure 7. 3D Visualization of Fire scene.

3.2.2. Moisture of Combustibles

Based on spectral analysis and the angle slope index, the moisture content of combustibles in the fire area can be achieved by using the multispectral remote sensing data from Sentinel-2's Band 4, Band 8, and Band 11. Additionally, based on the Normalized Difference Vegetation Index (NDVI), vegetation cover in the fire area can be obtained using Band 4 and Band 8, and the results after error correction are shown in Figure 8. The results of the moisture content of combustibles, overlaid with vegetation cover data masks to remove background environmental impacts, are shown in Figure 9. After excluding outliers, the average moisture content is 0.583±0.145, minimum and maximum being 0.013 and 1.355 respectively. Values below 0.357 account for 1.5%, values between 0.362 and 0.795 account for 89.2%, with moisture content concentrated between 0.388 and 0.682, accounting for 77.7%. Pixels near the fire line, affected by the intensity of the fire, mostly have moisture content ranging from 0 to 0.232, with the highest moisture content in adjacent areas exceeding 1. According to Li et al., the same type of vegetation has higher moisture content in undergrowth and the canopy layer due to the physiological moisture of sprouting new leaves and branches, while ground cover has lower moisture content due to the adherence of dead leaves and branches, and it varies significantly with weather conditions [27]. In this study, the canopy vegetation moisture content inverted using Sentinel-2 should be higher than the actual moisture content of combustibles; however, this deviation should converge due to the high temperatures and smoke at the fire scene.

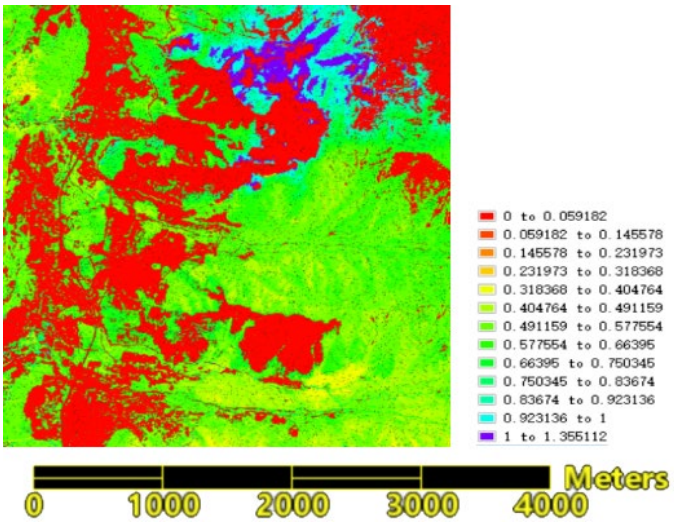

Figure 8. Normalized vegetation index after error correction.

 doi:10.20944/preprints202408.1458.v1

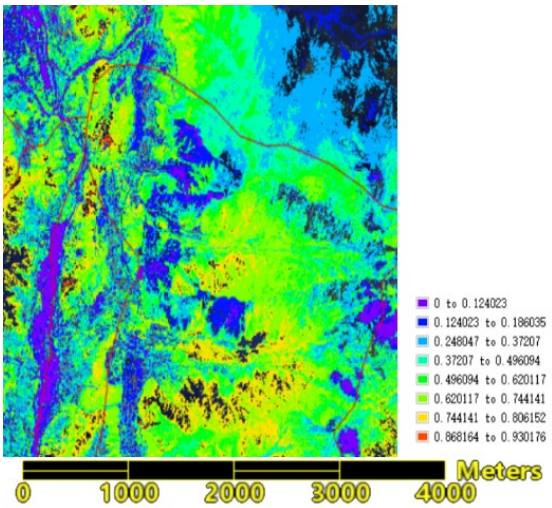

Figure 9. The estimated moisture content in combustibles.

3.2.3. Slope Data from DEM

The third-order inverse-distance squared total differential method with a 3×3 local moving window size was used to compute the 30-meter STER GDEM data. The results are shown in Figure 10. From the interpreted statistical data, the minimum and maximum is 0.0049 and 88.76 respectively, the average slope value is 24.19±15.36, with a high standard deviation. The high standard deviation is most likey due to the fire area featuring high mountains, steep slopes, less gentle slopes, and obvious relief features. There are 267,043 pixels with slopes ranging from 0 to 59 degrees, accounting for 99.4% of the total, and 1,668 pixels with slopes between 80 to 88.76 degrees, accounting for 0.6%.

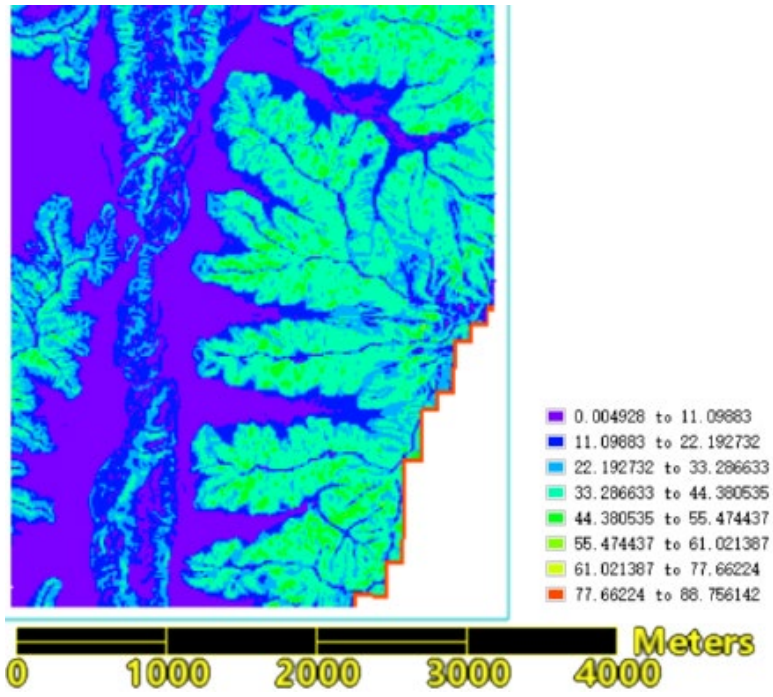

Figure 10. Result of Slope extraction from DEM.

3.2.4. Wind Speed

Wind factors are divided into wind direction and wind speed. Generally, the wind direction is the direction of the fire front's spread and the wind speed directly affects the spread speed of the fire. The higher the wind speed, the faster the fire spreads in the direction of the wind, and the larger the

 doi:10.20944/preprints202408.1458.v1

wind speed correction factor [28]. At 2021-04-24T04:00:00Z, the wind speed was 1.44 m/s to the north and -0.78 m/s to the east (or 0.78 m/s to the west), resulting in an actual wind direction from the northwest with a wind speed of 1.638 m/s, forming an angle of 241.56° with the uphill direction. The correction factors for wind force in various directions are shown in Table 5.

Table 5. Correction Factors of Wind force in all directions.

uphill	downhill	leftward	rightward	Wind direction
$e^{0.1783v\cos\theta}$	$e^{0.1783v\cos(180-\theta)}$	$e^{0.1783v\cos(\theta+90^{\circ})}$	$e^{0.1783v\cos(\theta-90^{\circ})}$	$e^{0.1783v}$
0.870	1.149	1.293	0.774	1.339

3.2.5. Correction Factor for Combustible Material Type

Although a combustible material correction factor, K_S, was considered in Wang Zhengfei model for fire spread prediction, detailed classifications of combustible material types were unavailable, which makes precise calculations difficult if not impossible [29]. Zhang developed an empirical constants table for the impact factors of combustible material types [30], as shown in Table 6.

Table 6. Correction coefficient (K_S) of combustible types on forest fire spreading speed.

combustible type	Correction factor K_S	Combustible type	Correction factor K_S
Coniferous forest	0.4	Secondary forest	0.7
Spread pine needles	0.8	Red pine, Yunnan pine, Huashan pine, etc	1.0
Dead branches and fallen leaves	1.2	Thatch grass and weeds	1.6
Sedge and dwarf birch	1.8	Pasture grassland	2.0

According Tang et al. [31], the fire area is mostly primary forest, with vegetation coverage exceeding 80%, predominantly consisting of broadleaf forests such as eucalyptus. Secondary forests are typically dominated by broadleaf species, have mixed stand structures, and include a mixture of trees and shrubs. By comparing with the types of combustibles listed in Table 6, the type of combustibles in the fire scene area is most similar to the secondary forest listed in the table. Therefore, the correction factor of 0.7, corresponding to the secondary forest in the table, is taken as the combustible type correction factor for the fire spread prediction.

3.3. Prediction of RS Enabled Fire Spreading

Slope and aspect of terrain are key factors affecting the speed of wildfire spread. Typically, fires spread slower downhill and faster uphill. The steeper the slope, the easier it is for water to run off, making the combustibles drier and indirectly accelerating the spread of the fire. This also affects the moisture content of the combustibles: sunlit slopes receive more sunlight, making the combustibles less moist and more flammable; conversely, the combustibles on shaded slopes retain more moist, making them less flammable. Therefore, based on the three-dimensional visualization of the fire scene (Figure 7), the positions of different fire lines on uphill, downhill, left level slopes, right level slopes, as well as the wind direction, were determined. Targeted fire speed simulations for each direction were also conducted.

As shown in Figure 7, the north wind direction coincides with the direction of the left level slope and the east wind (which is negative) coincides with the downhill direction. The actual wind direction is from the northwest. Because burned areas generally do not reignite and form a barrier, they are not included in predictions for fire spread speeds. On the eastern line, sectors 1, 2, and 3 have intense fires and are located on uphill terrain with steep slopes, leading to faster spread speeds. Therefore, the fire spread speeds for uphill, left level slope, and right level slope at the top of the fire line of sector 1 are predicted, while for fire line of sectors 2 and 3, the spread speeds for uphill and

 doi:10.20944/preprints202408.1458.v1

right level slope directions are predicted. For fire line of sector 4, which is at the base of the mountain with a relatively low terrain slope, the fire spread speed for uphill, left level slope, downhill, and wind direction is predicted. Other fire spread predictions include downhill and wind direction for sectors 5, and downhill, left level slope, right level slope, and wind direction for sector 6.

After incorporating the remote sensing data and temperature effects associated with different elevations, the prediction results are as follows:

In Fire Line 1 area, there are 15 adjacent pixels, with one outlier removed. The vegetation moisture content is below 0.01, with the minimum and maximum slope being 13.24°and 42.34°respectively. The maximum speed for uphill, left level slope, and right level slope is 11.782, 0.939, and 0.562 m/min respectively.

In Fire Line 2 area, there are 32 adjacent pixels, with one outlier removed. Five pixels have vegetation moisture content below 0.01, with the maximum reaching 1.008. Slopes are above 34.5°, with the maximum slope being 45.01°. The maximum fire spread speed for uphill and right level slope is 13.858 and 0.562 m/min, respectively.

In Fire Line 3 area, there are 55 adjacent pixels, with five outliers removed. Nineteen pixels have vegetation moisture content below 0.01, while the majority of the remaining pixels are around 0.5, with the highest value reaching 0.911. The minimum slope is 15.500°and the maximum slope is 46.544°. The maximum fire spread speed for uphill and right level slope speed is 16.527 and 0.562 m/min, respectively.

In Fire Line 4 area, there are 26 adjacent pixels, with nine pixels having a moisture content below 0.01, and the rest between 0.483 and 0.987. Slopes are above 33°, with the maximum slope being 41.770°. The maximum speed for uphill, left level slope, downhill, and wind direction is 11.254, 0.939, 1.702, and 17.319 m/min, respectively.

In Fire Line 5 area, there are 9 adjacent pixels, with moisture content between 0.5 and 0.6. The slopes range from 11.984° to 12.550°. The maximum downhill speed is 1.061 m/min and the maximum wind direction speed is 1.587 m/min.

In Fire Line 6 area, there are 47 adjacent pixels, with one outlier removed. Ten pixels have vegetation moisture content below 0.01, the rest between 0.415 and 0.733. Slopes are below 28°, with the minimum slope being 1.024°. The maximum fire spread speed for downhill, left level slope, right level slope, wind direction is 1.378, 0.939, 0.562, and 5.669 m/min, respectively.

Given the limitations of time and spatial resolution associated with satellite RS images, the sudden nature of forest fires, and the accuracy of RS inversion parameters, the fire spread range one hour later is based on the statistical values of forest fire spread speed results in each direction mentioned above. The results are shown in Table 7 and Figure 10.

Table 7. Maximum spread distance after 1 hour in all directions (unit: meter).

Location of fire line	uphill	left	Right	downhill	Wind direction
Zone 1	706.91	56.31	33.70		
Zone 2	831.47		33.70		
Zone 3	991.62		33.70		
Zone 4	675.25	56.31		102.13	17.32
Zone 5				63.67	95.22
Zone 6		56.31	33.70	82.69	340.14

It is evident that the fire spread speed is the fastest in the uphill direction, resulting in the longest spread distance, while the spread distances on the left level slope and the right level slope are essentially the same. Note that fire line 6 area shows a greater spread distance in the wind direction.

The RS enabled fire spread prediction can provide critical information for firefighters to effectively combat fires. In the case of Mianning fire, based on the land cover type map before the forest fire (from the National Basic Geographic Information Center) (as shown in Figure 11) and high-resolution remote sensing imagery (Sentinel-2), the west side of the forest fire borders the Jingkun Expressway (as shown in Figure 12), which is non-forested and forms a barrier. Typically, a forest

 doi:10.20944/preprints202408.1458.v1

fire will extinguish on its own upon encountering non-combustible materials unless spot fires occur (which would cause the fire to jump to other mountain tops). Therefore, based on the RS-enabled fire spread prediction, it is recommended that defense and firefighting efforts should concentrate on the eastern sectors 1, 2, and 3, as well as the northern and eastern areas of sector 4 on the western line.

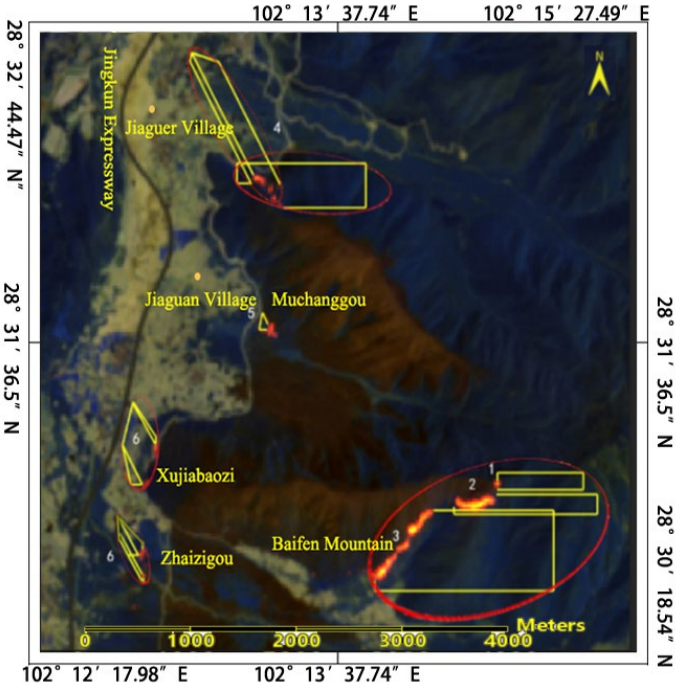

Figure 11. Prediction of fire line spread distance one hour later.

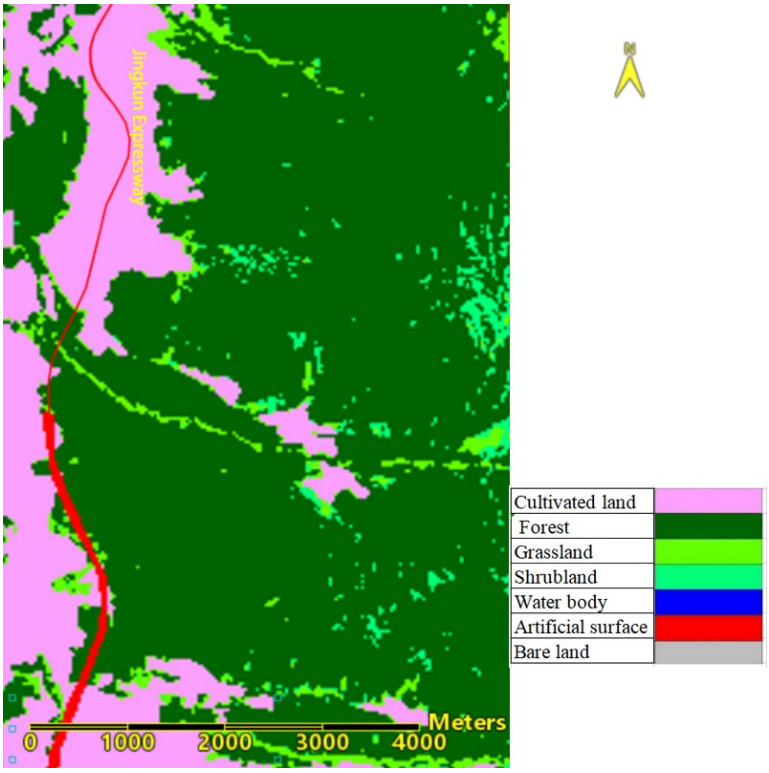

Figure 12. Fire area land cover type map.

 doi:10.20944/preprints202408.1458.v1

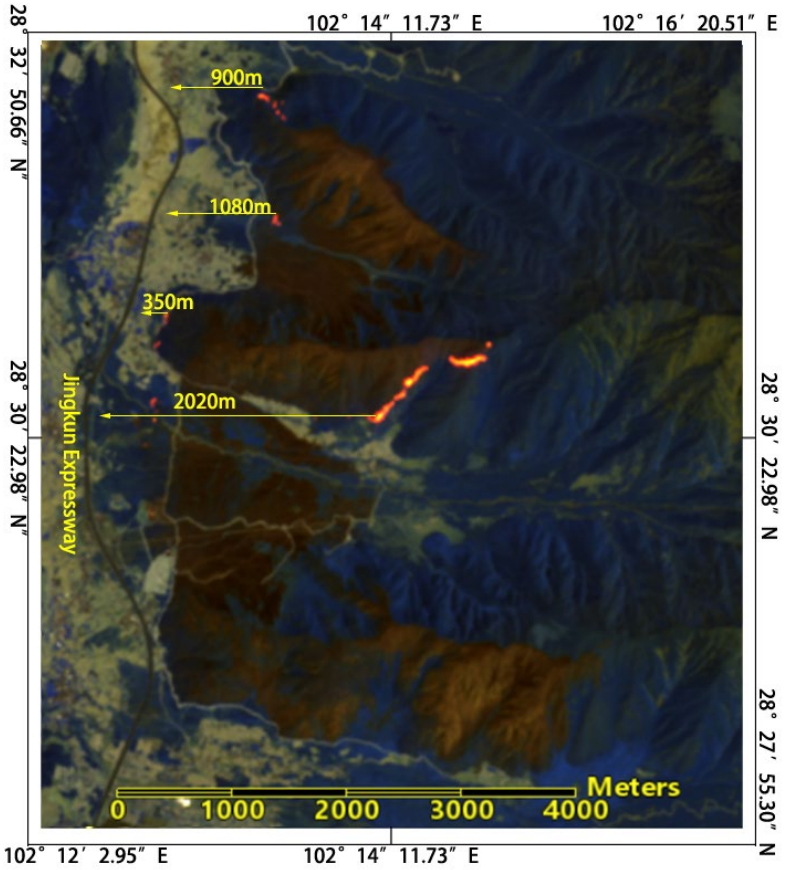

Figure 12. Map of the fire line and Jingkun Expressway locations.

3.4. Comparison of RS Enabled Fire Spread Prediction with Actual Mianning Fire

According to the hourly meteorological data for Mianning County on 2021-04-24 shown in Table 2, between T4:00 and 5:00, the wind direction and speed changed from north at 1.44 m/s and east at -0.78 m/s to north at 1.48 m/s and east at -0.54 m/s, indicating relatively stable conditions. Based on the maximum spread distances in each direction shown in Table 7, the average increase in visible fire area was calculated to be 3.257 hm²(square hectare) per 10 minutes within one hour. Analysis of the dynamic changes in the visible fire area of the Mianning forest fire monitored by Himawari-8 satellite every 10 minutes from 2021-04-24 T03:40 to 2021-04-24 T05:00 (UTC) (Figure 13) shows a significant increase in visible fire area, with an average increase rate of 3.297 hm² per 10 minutes. This rate can be considered consistent with the results simulated by the RS-enabled forest fire spread model. The small discrepancy may be likely due to the differences in spatial resolution between remote sensing images.

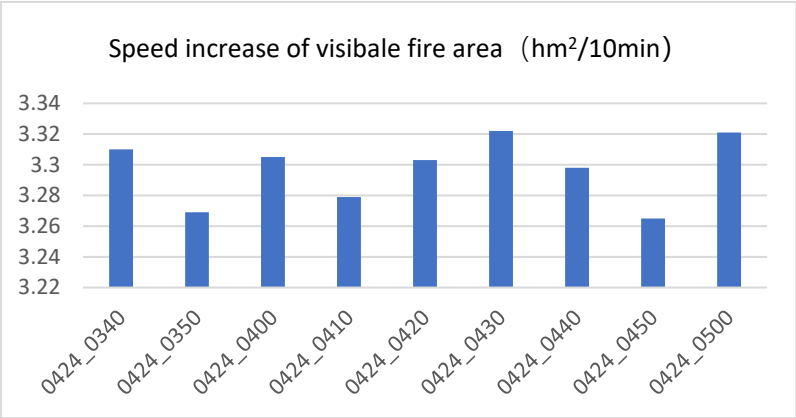

 doi:10.20944/preprints202408.1458.v1

Figure 13. Dynamic map of the increase in visible fire area at the Mianning 4.24 forest fire site monitored by Himawai-8 satellite.

According to the analysis of the remote sensing imagery of fire spots from the Himawari-8 satellite on April 24 from 3:40 to 5:00 (Figures 14 and 15), the fire monitoring points progressed westward from Jiaguan Village and did not cross the Jingkun Expressway (102°12′38″E); it extended eastward from Baifen Mountain and northward from Dashuigou (as shown in rectangles 1, 2, 3, and 4 in Figure 15), consistent with the trend observed in the forest fire spread model simulations.

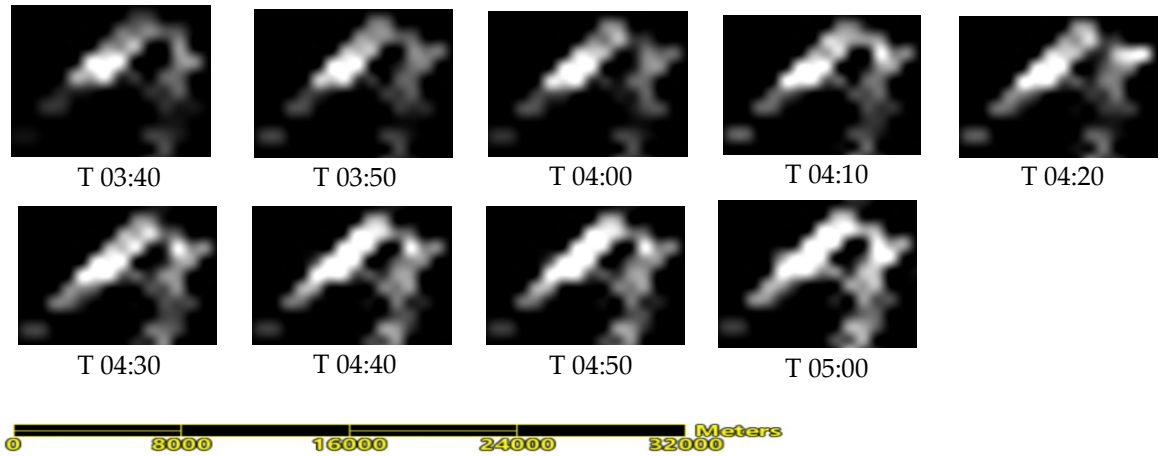

Figure 14. Himawari-8 remote sensing imagery brightness temperature anomaly monitoring results from 2021-04-24 T03:40 to 2021-04-24 T05:00.

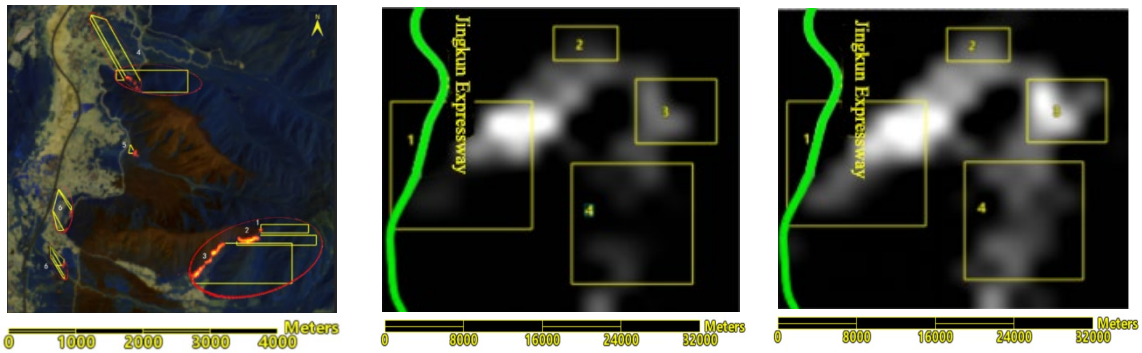

(a) (b) (c)

Figure 15. Comparison between forest fire spread model simulation results and remote sensing monitoring.(a) Forest fire spread simulation results; (b) Himawari-8 remote sensing imagery brightness temperature anomaly monitoring at T03:40. (c)Himawari-8 remote sensing imagery brightness temperature anomaly monitoring at T05:00.(Green line is the Jingkun Expressway, yellow line is the comparison region).

Using the mid-infrared image from Gaofen-4 IRS (GF4_IRS_E103.0_N29.3_20210424 _L1A0000374570), taken 58 minutes after the Sentinel-2 image at T03:45, the anomaly temperature perception in the forest fire area was studied to verify the results of the RS enabled forest fire spread. The Gaofen-4 data were collected at 04:43:42 on April 24, and the brightness temperatures derived from the mid-infrared band are shown in Figure 16. Using the 20-meter resolution remote sensing image from Sentinel-2 as a base image, the Gaofen-4 infrared IRS image was geometrically corrected and precisely registered. The two images were overlaid with the Gaofen image on top, with the top image's transparency being set to 50%, as shown in Figure 17. Upon enlargement, the boundary of the anomaly temperature and the predicted forest fire spread area overlapped as shown in Figure 18. The results clearly show that the predicted forest fire spread area (Regions 1-6) essentially aligns well

 doi:10.20944/preprints202408.1458.v1

with the brightness temperature anomaly boundary detected by the Gaofen-4 IRS image. The small discrepancies may have been caused by factors such as smoke from the fire, lower mid-infrared image resolution, and firefighting activities.

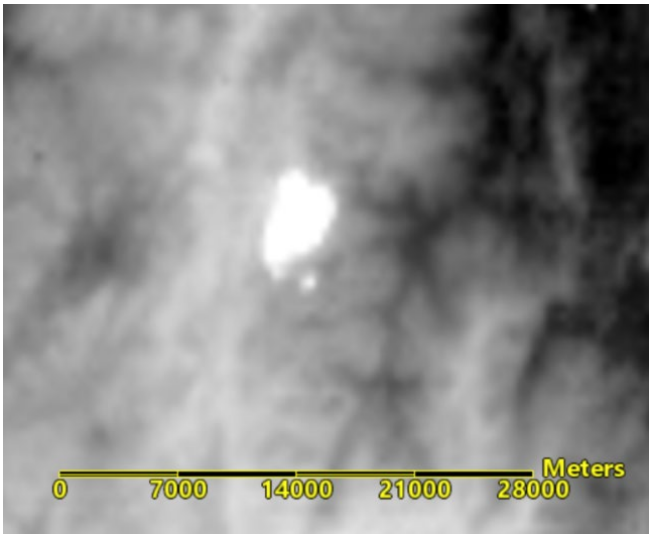

Figure 16. Gaofen-4 mid-infrared brightness temperature map.

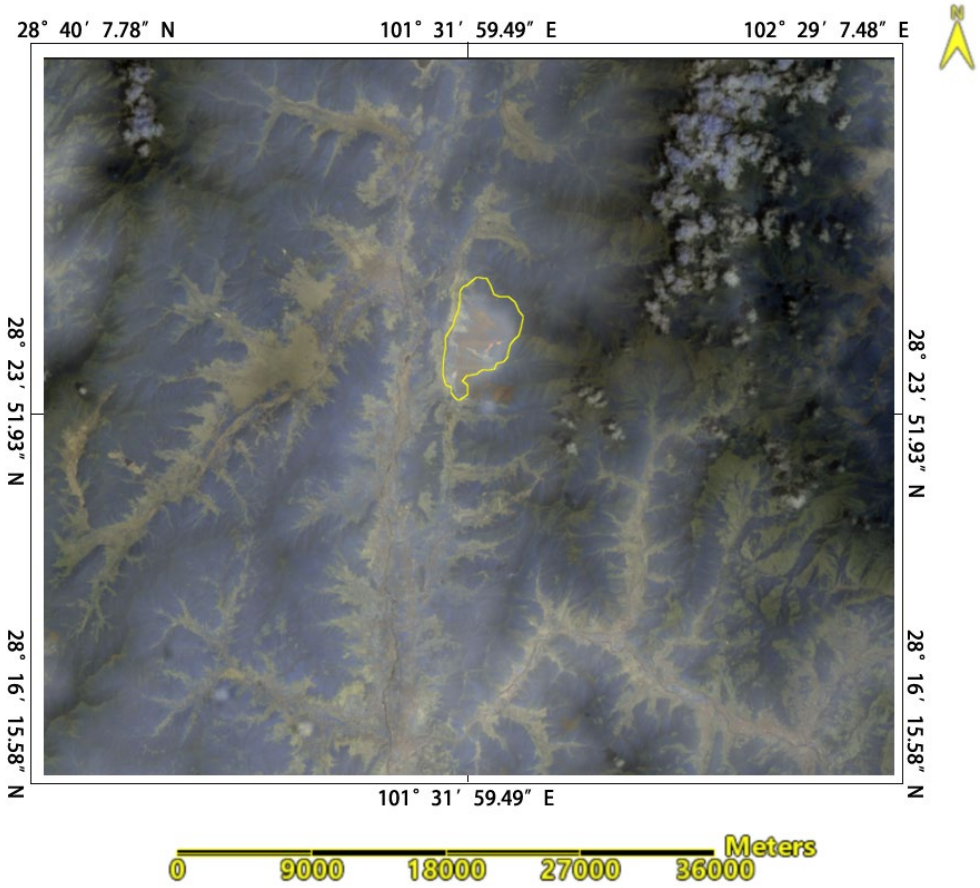

Figure 17. Gaofen-4 mid-infrared brightness temperature map (yellow indicates the boundary of abnormal brightness temperature).

 doi:10.20944/preprints202408.1458.v1

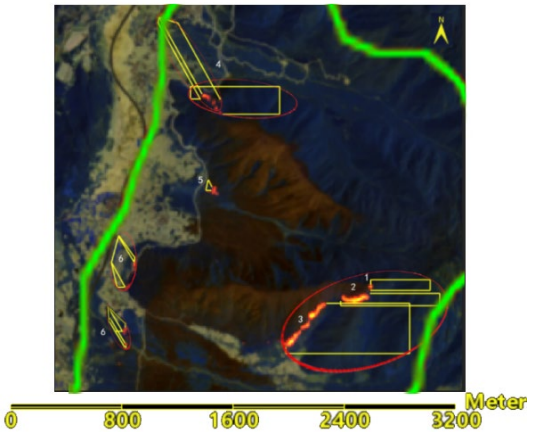

Figure 18. Overlay results of the abnormal brightness temperature boundary and the predicted forest fire spread area (green line indicates the abnormal brightness temperature boundary, yellow line indicates the forest fire spread area).

The deduced spread area is also consisitent with the results of Tang Y. et al.'s research [31] and historical archives.

The above analysis shows that the predicted spread area of the model generally matches the actual spread results, demonstrating the accuracy and reliability of the RS enabled fore fire spread model for predicting the forest fire development, particularly in those fires occurring in the difficult-to-access areas.

3.5. Further Considerations

Given the limitations in time and spatial resolution of remote sensing satellite imagery, which prevent real-time acquisition of forest fire imagery data, future research could further investigate improved models of forest fire spread. This could include incorporating key factors such as surface temperature and combustible biomass that affect the speed of fire spread. Additionally, studying RS collection methods for these influencing factors across different satellite data could further enhance the model's applicability. As a crucial component of intelligent forest fire management, advanced RS technology is expected to further enhance the accuracy and precision of forest fire prediction.

4. Conclusions

The spread speed of forest fires is a crucial factor in predicting forest fire behavior. Many factors influence the spread speed. This study examines the impact of temperature changes at different altitudes on the spread speed, with the model correlation coefficient reaching 0.92. This indicates that altitude significantly affects the initial spread speed of forest fires and can be an important factor in estimating spread speed. Additionally, this study obtained parameters required for the forest fire spread model by retrieving Sentinel-2 RS images of a forest fire: the moisture content of combustibles in the forest area inverted based on spectral analysis and the angle slope index; both slope and altitude data calculated with the third-order inverse distance squared full difference method and using a 3×3 local moving window size, based on the DEM elevation model. Fire spot detection during the forest fire was conducted using both Himawari-8 and Gaofen-4 satellite data and served as a basis for evaluating the accuracy of the fire spread model simulation results. An analysis of the dynamic changes in the visible fire area of the Mianning forest fire, monitored by the Himawari-8 satellite at 10-minute intervals from 03:40 to 05:00 on April 24, 2021, showed an average increase in the visible fire area of 3.297 hm^2 per 10 minutes, which is basically consistent with the results simulated by the RS-enabled forest fire spread model. The trends in the remote sensing monitoring sequence images of the fire spots also corresponded with the results simulated by the RS-enabled forest fire spread model. Based on the mid-infrared images from the Gaofen-4 IRS, taken 58 minutes after the Sentinel-

 doi:10.20944/preprints202408.1458.v1

2 images, to identify the anomaly temperature in the forest fire area, the results of the forest fire spread were validated. The results show that the predicted forest fire spread area aligns well with the brightness temperature anomaly boundary detected by the Gaofen-4 IRS images. The dual validation results show that the spread area deduced by the RS-enabled forest fire spread model in this study generally matches the actual spread results and can serve as a basis for assessing the fire situation.

The continuous advancement of satellite remote sensing interpretation technology can effectively address the challenges in obtaining the necessary parameters for forest fire spread prediction models and the poor universality of algorithms. Using RS-enabled forest fire prediction models to deduce the trends of forest fire spread is expected to effectively enhance the scientific basis for fire assessment and proactive defense planning.

Author Contributions: Conceptualization: G.Z. and P.L.; methodology, collected the study data, formal analysis and writing—original draft: P.L.; funding acquisition, writing—review, comments and editing: P.L. ALL authors have read and agreed to the published version of the manuscript.

Funding: This research was funded by a project supported by the Scientific Research Fund of Hunan Provincial Education Department under Grant 23B0244 and 22A0194, the Science and Technology Innovation Platform and Talent Plan Project of Hunan Province under Grant 2017TP1022, the Natural Science Foundation of Hunan Province under Grant 2024JJ7645 and Field Observation and Research Station of Dongting Lake Natural Resource Ecosystem, Ministry of Natural Resources.

Data Availability Statement: The data presented in this study are available on request from the corresponding author.

Acknowledgments: We thank the Department of Emergency Management of Hunan Province for their provision of forest fire hotspot data.

Conflicts of Interest: The authors do not have conflict of interest in this study.

References

1. Jiang, B.; Chen, T.; et al. Study on forest fire spread model based on remote sensing interpretation. *China Emergency Rescue* **2021**, *3*, 11-16.
2. He, W.; Bai, J. Application and prospects of the Canadian Forest Fire Behavior Prediction System. *World Forestry Research* **2014**, *3*, 82-86.
3. Sun, X.; Fan, W.; Li,M. Study and implementation of forest fire spread models. *Forestry Machinery and Woodworking Equipment* **2009**, *5*, 16-19.
4. Zhang, J.; Liu, B. Prediction of fire behavior of mixed combustibles on the forest floor of Pinus koraiensis and Quercus mongolica under flat and windless conditions using the generalized Rothermel model. *Chinese Journal of Applied Ecology* **2012**, *6*, 1495-1502.
5. Wang, Z. Measurement method for the initial spread rate of wildfires. *Mountain Research* **1983**, *1(2)*, 42-51.
6. Mao, X.; Xu, W. Study on calculation methods for forest fire spread rate. *Liaoning Meteorology* **1991**, *1*, 9-13.
7. Zhang, X.; Liu, P.;Wang,X. Research on the improvement of Wang Zhengfei's forest fire spread model. *Shandong Forestry Science and Technology* **2020**, *50(1)*, 1-6,40.
8. Fan, J.; Gao, J. *Middle School Geography(First semester of The seventh grade)*, 1st ed.; People's education press: Beijing, China, May, 2012; pp. 56.
9. Charles, W.R.; Dudley, W. Lambert Absorption Coefficients of Water in the Infrared.*Journal of the Optical Society of America* **1971**, *10*, 1316.
10. Carter, G.A. Primary and Secondary Effects of Water Content on The Spectral Reflectance of Leaves. *American Journal of Botany* **1991**, *78*, 916-924.
11. Deng, B.; Yang, W.;Mu,N.;et al. Study on vegetation water content based on spectral analysis and angle slope index. *Spectroscopy and Spectral Analysis* **2016**, *36(8)*, 2546-2552.
12. Khanna,.; Alicia,P.O.; Michael,L. Whiting, et al. Development of angle indexes for soil moisture estimation, dry matter detection, and land-cover discrimination. *Remote Sensing of Environment: An Interdisciplinary Journal* **2007**, *109(2)*, 154-165.
13. Tucker, C.J. Remote sensing of leaf water content in the near infrared. *Remote Sensing of Environment* **1980**, *10(1)*, 23-32.
14. Lei, J.; Yang, W.;Yang,X.;et al. Vegetaion Canopy Moisture Inversion based on Improved Distance Projection Ratio Index. *People's Yangtze River* **2021**, *52(09)*, 113-118.

 doi:10.20944/preprints202408.1458.v1

15. Liu, X. Analysis and evaluation of error in rule grid digital elevation model interpretation algorithms. Master, Wuhan University, Wuhan, 2002.
16. Tang, G.; Yang,Q.; Zhang, Y.; et al. Accuracy of ground slope extraction from DEMs at different scales—A test in the loess hilly gully region. *Bulletin of Soil and Water Conservation* **2001**, *21(1)*, 53-56.
17. Liu, X.; Gong, J.; Zhou,Q.; et al. Analysis of accuracy of DEM slope and aspect algorithms. *Journal of Surveying and Mapping* **2004**, *33(3)*, 258-263.
18. Hao, Z. Comparison of DEM slope and aspect algorithms under different terrains. *Hydropower and Energy Science* **2011**, *29(6)*, 68-70.
19. Sharpnack, D.A.; Akin, G. An algorithm for computing slope and aspect from elevations. *Photogrammetric Engineering* **1969**, *35*, 247-248.
20. Chen, N.; Wang, Q. Analysis of the application range of 6 slope extraction algorithms—A study in the loess hilly gully region. *Mapping Information and Engineering* **2006**, *31(4)*, 20-21.
21. Li, F.; Li, J.; Zhang, Q. Comparative study of DEM slope and aspect extraction algorithms. *Anhui Agricultural Sciences* **2008**, *36(17)*, 7355-7357.
22. Jiang, J.; Li, Y.; Wang, Y. Comparative analysis of 6 slope extraction algorithms based on DEM—A case study of Qingdao City, Shandong Province. *Mapping and spatial geographic information* **2018**, *41(2)*, 195-199,206.
23. He, Z.; Zhao, M. Comparison of slope extraction algorithms for different geomorphological types. *Bulletin of Soil and Water Conservation* **2008**, *28(6)*, 126-129.
24. Liu, S.; Li, X.; Qin, X.; et al. Adaptive threshold segmentation of ignition points in GF-4 PMI images. *Journal of Remote Sensing* **2020**, 24(3), 215-225.
25. Roberts G. J. and Wooster M. J., Fire detection and fire characterization over Africa using Meteosat SEVIRI. *IEEE Transactions on Geoscience and Remote Sensing*, 2008, 46(4), 1200–1218.
26. Giglio L., Schroeder W., and Justice C. O., The collection 6 MODIS active fire detection algorithm and fire products, *Remote Sensing And Environment*, 2016, 178, 31–41.
27. Li, C. Study on the relationship between forest fuel moisture content and fire risk level. *Yunnan Forestry Investigation and Planning* **1994**, *4*, 37-42.
28. Mao, X. The effect of wind and terrain on the spread speed of forest fires. *Journal of Applied Meteorology* **1993**, *1*, 100-104.
29. Xue, H.; Hu, X. Exploiting Sensor Spatial Correlation for Dynamic Data Driven Simulation of Wildfire. Proc. ACM/IEEE/SCS Workshop on Principles of Advanced and Distributed Simulation (PADS), Zhangjiajie, China, 15-19 July 2012.
30. Zheng, H. Calculation and application of fire field parameters. *Agricultural Press* **1988**, *4*, 8-9.
31. Tang, Y.; Wang, L.; Deng, C.; et al. High-resolution remote sensing technology assists in emergency firefighting and hidden hazard prediction of forest fires—A case study of the "4·20" forest fire in Mianning. *Journal of Remote Sensing* **2021**, *25(9)*, 2015-2026.